



**HAL**  
open science

## Photonic THz mixers based on iron-doped InGaAs embedded in a plasmonic microcavity

Charbel Tannoury, Victor Merupo, Giuseppe Di Gioia, Vanessa Avramovic, David Troadec, Jean-François Lampin, Guillaume Ducournau, Steffen Breuer, Björn Globisch, Stefano Barbieri, et al.

► **To cite this version:**

Charbel Tannoury, Victor Merupo, Giuseppe Di Gioia, Vanessa Avramovic, David Troadec, et al.. Photonic THz mixers based on iron-doped InGaAs embedded in a plasmonic microcavity. *APL Photonics*, 2023, 8 (11), pp.116101. 10.1063/5.0153046 . hal-04268627

**HAL Id: hal-04268627**

**<https://hal.science/hal-04268627>**

Submitted on 2 Nov 2023

**HAL** is a multi-disciplinary open access archive for the deposit and dissemination of scientific research documents, whether they are published or not. The documents may come from teaching and research institutions in France or abroad, or from public or private research centers.

L'archive ouverte pluridisciplinaire **HAL**, est destinée au dépôt et à la diffusion de documents scientifiques de niveau recherche, publiés ou non, émanant des établissements d'enseignement et de recherche français ou étrangers, des laboratoires publics ou privés.

# Photonic THz mixers based on iron-doped InGaAs embedded in a plasmonic microcavity

Charbel Tannoury<sup>1†</sup>, Victor Merupo<sup>1†</sup>, Giuseppe Di Gioia<sup>1</sup> Vanessa Avramovic<sup>1</sup>, D. Troadec<sup>1</sup>, J-F. Lampin<sup>1</sup>, Guillaume Ducournau<sup>1</sup>, Steffen Breuer<sup>2</sup>, Björn Globisch<sup>2,3</sup>, Stefano Barbieri<sup>1</sup>, Robert B. Kohlhaas<sup>2</sup> and Emilien Peytavit<sup>1\*</sup>.

<sup>1</sup>Univ. Lille, CNRS, Univ. Polytechnique Hauts-de-France, UMR 8520 - IEMN, F-59000 Lille, France

<sup>2</sup>Fraunhofer Institute for Telecommunications, Heinrich Hertz Institute, Einsteinufer 37, 10587 Berlin, Germany

<sup>3</sup>Technische Universität Berlin, Institut für Festkörperphysik, Hardenbergstr. 36, 10623 Berlin, Germany

\*Corresponding author: [emilien.peytavit@iemn.fr](mailto:emilien.peytavit@iemn.fr)

† *These authors contributed equally to this work*

## Abstract

We present an optoelectronic mixer for the terahertz (THz) frequency-domain based on an iron-doped InGaAs layer integrated in a plasmonic microcavity. We show that this structure, under 1550-nm-wavelength illumination, allows for more than 70% absorption efficiency in a 220 nm-thin InGaAs absorber and very high  $R_{off}/R_{on} > 1000$ . It leads to THz mixers driven by 1550-nm lasers showing conversion loss as low as  $\sim 30$  dB at 300 GHz. Therefore, this design is very promising for application as receivers in high-data-rate wireless telecom, in cw-THz spectrometers, or in photonics-enabled THz spectrum analyzers.

## 1 Introduction

Frequency mixers are an essential component of RF and THz systems. For example, heterodyne receivers using Schottky diode mixers pumped by local oscillators based on multiplier chain, have opened the way to THz sensors with fW-power-level sensitivity working at room temperature<sup>1,2</sup>. Besides these promising developments based on all-electronic devices and driven largely by applications in astronomy, earth and planetary science<sup>3</sup>, numerous studies on THz sources and detectors using photonic techniques have been performed during last years in the wake of the continuous improvement of near-infrared lasers sources at wavelengths between 780 and 1550 nm. Today, laser-driven sources and detectors are a key

components of commercial THz spectrometers<sup>4,5</sup> and have enabled the race to high data rates in THz wireless communications by bridging the gap between optical fibers and wireless communications technologies<sup>6</sup>.

Photonic-based detection of continuous THz waves is also based on frequency mixing since, as illustrated in Figure 1a, the THz input wave is down-converted to an intermediate frequency  $f_{IF}$  in a photoconductor illuminated by an optical signal modulated at a frequency  $f_{LO}$  such that  $f_{IF} = |f_{LO} - f_{THz}|$ . More precisely, in the case of commercial THz spectrometers, the scheme is called homodyne detection<sup>7</sup>, since the same optical beat note of two slightly detuned laser lines is used for generating and detecting THz radiation, implying  $f_{THz} = f_{LO}$ . Optoelectronic mixers using a laser-based local oscillator (LLO) have indeed numerous advantages as compared to existing all-electronics technologies. First, the LLO frequency is widely tunable up to a few THz due to the huge bandwidth in the optical-domain. This paves the way for the development of THz-frequency-band spectrum analyzers with applications in high-resolution THz spectroscopy or electrical characterization of analog devices for 5G/6G communications systems. In addition, the LLO-signal is compatible with standard optical fibers, which are lightweight and immune to electromagnetic interference. This is particularly advantageous for antenna arrays, which require the distribution of the LLO signal to each individual antenna. The same considerations are valid for integrated THz antenna arrays, which could be realized by on-chip photonic circuits. To take advantage of the low-cost, reliable and efficient telecom-fiber components, 1550 nm need to be used as the operating wavelength. At the same time, several challenges remain to be addressed to exploit the full potential of photonic-assisted instruments for RF/THz applications. The first one is the development of LLOs whose frequency stability and noise approach that of electronic sources while remaining largely tunable<sup>8-13</sup>. The second challenge lies in increasing the performance of optoelectronic mixers working at 1550 nm in terms of conversion loss and noise temperature, to become competitive with electronic solutions. Hitherto, photoconductors used as heterodyne or homodyne detectors in THz systems are based on planar, interdigitated electrode capacitors patterned on low-carrier lifetime materials. Photoconductors suitable for optical excitation at telecom wavelengths are typically made of low temperature grown-InGaAs/InAlAs MQWs<sup>14</sup> or Fe-doped InGaAs layers<sup>15,16</sup>. The advantage of planar electrodes is their intrinsically low electrical capacitance allowing for efficient operation up to a few THz. Unfortunately, these electrodes come with a large conversion loss of  $\sim 50 - 60$  dB<sup>17,18</sup>, which is far away from the

best electronic mixers whose conversion loss can be as low as 12 dB<sup>1</sup> when they are integrated in a waveguide and operate in a reduced frequency bandwidth.

In this work, we present the design, fabrication and characterization of an ultrafast photoconductor embedded in a plasmonic microcavity designed for 1550-nm operation. This design improves the photoconductance and conversion efficiency by reducing the electrode spacing while maintaining high optical absorption and carrier collection efficiency. The photoconductor is based on a high-dark-resistivity and sub-picosecond-carrier-lifetime iron-doped InGaAs layer. With this design, we demonstrate conversion losses lower than ~30 dB for frequencies up to 320 GHz.

## 2. Results

### *Optoelectronic mixing by a photoconductor: design rules and minimum conversion loss.*

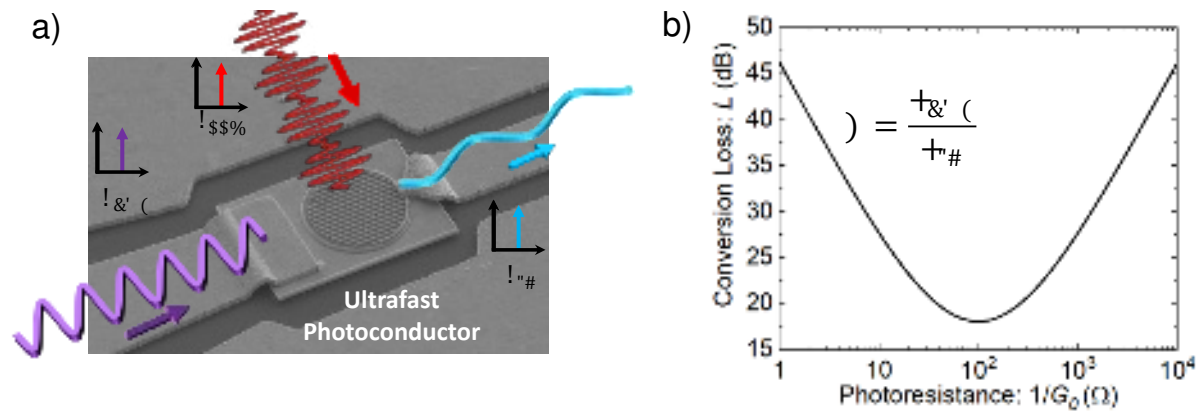


**Fig. 1** Details of the optoelectronic heterodyne THz receiver. (a) SEM image illustrating the down-conversion of an incoming THz frequency signal (purple) by mixing with a laser-based local oscillator (red) in a photoconductor. The output of the mixing process is the IF-signal (blue). (b) Conversion loss vs photoresistance of the photomixer calculated by using Eq. 1.

An ultrafast photoconductor illuminated by a light modulated at frequency  $\omega_{LO}$  can be modeled as a parametric conductance  $G(t) = G_0 + G_1 \cos(\omega_{LO}t)$ , since the charge carrier density in the device is driven by the intensity of the optical pump<sup>19</sup>. Here,  $G_0$  and  $G_1$  are the average and modulated parts of the photoconductance, respectively. In addition, since the frequency response of the photoconductor is governed by the carrier lifetime  $\tau$ ,  $G_1 = (G_0 - G_{dark})/\sqrt{1 + (\omega_{LO}\tau)^2}$ <sup>20</sup> with the dark conductivity  $G_{dark}$ . This parametric photoconductance generates mixing frequency terms at  $n\omega_{LO} \pm \omega_{THz}$ ,  $n$  being a positive integer, when biased by an input THz signal at frequency  $\omega_{THz}$ . As shown in the Supplementary Material, the

conversion loss  $L = P_{THz}/P_{IF}$  between the incident THz power and the IF output power at  $\omega_{IF} = |\omega_{LO} - \omega_{THz}|$  can be expressed by:

$$L \approx (1 + (\omega_{LO}\tau)^2) \frac{(1 + 2G_0R_L)^4}{(1 - G_{dark}/G_0)^2(G_0R_L)^2} \quad (1)$$

where  $R_L$ , the input impedance of the IF receiver, is assumed to be equal to the source impedance. As expected, it can be seen from (1) that the carrier lifetime sets the frequency band of the mixer and minimizing the ratio  $G_{dark}/G_0$  is essential in order to minimize the conversion loss. For 1550-nm-operation, photoconductors based on iron-doped InGaAs photoconductive material, which shows both sub-picosecond carrier lifetime and high dark resistivity<sup>16</sup> ( $\rho > 1 \text{ k}\Omega\cdot\text{cm}$ ), are likely to fulfill these requirements. In the best-case scenario, i.e.  $\omega_{LO}\tau \ll 1$  and  $G_{dark} \ll G_0$ , a minimum conversion loss  $L_{min} \approx 18 \text{ dB}$  is achieved at  $1/G_0 \approx 2R_L$  as seen in Figure 1b. It could reach  $L_{min} \approx 12 \text{ dB}$  if IF and THz filters were added on each side of the photoconductance. If  $R_L = 50 \Omega$ ,  $L_{min}$  is obtained when  $G_0 = 10 \text{ mS}$ , a value 25-times larger than for state-of-the-art planar photoconductors. Please note that this is still much larger than the theoretical limit in conversion loss of 3.9 dB reached with an ideal resistive mixer ( $G_{on} \approx +\infty$ ) with matching loads working in pulsed mode at  $\omega_{LO}$  and 50 % duty cycle<sup>21</sup>. It is also still well above state-of-the-art electronic mixers which offer conversion loss around 12 dB up to 1 THz thanks to a careful electromagnetic design of IF and THz filters, which leads to a reduced tuning bandwidth around 10%<sup>1</sup>.

### ***InGaAs:Fe-based plasmonic cavity photoconductors for efficient optoelectronic mixing***

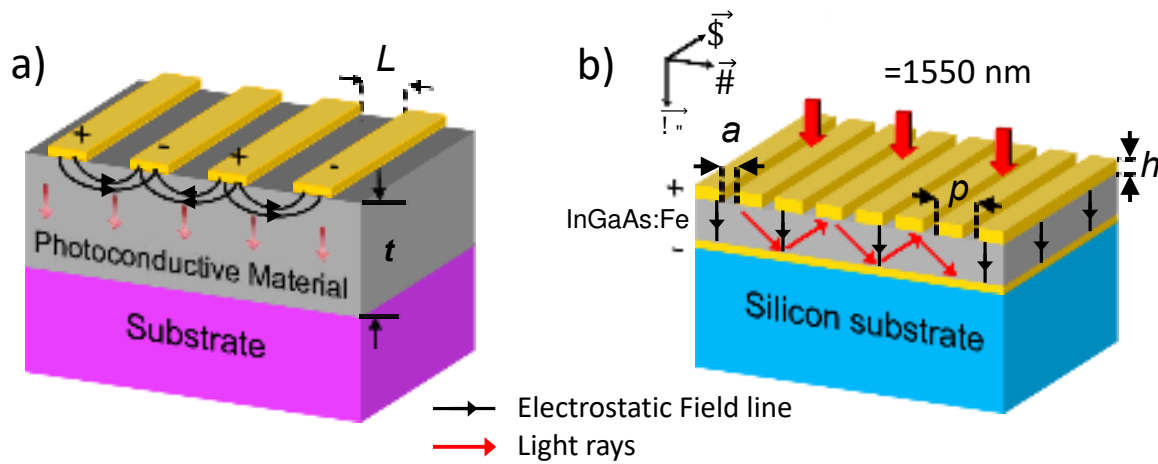


**Fig. 2** Schematic of the plasmonic microcavity photoconductor. (a) State-of-the-art, planar, interdigitated-electrode photoconductor.  $L$  is the electrode spacing and  $t$  denotes the thickness of the photosensitive layer.

**b) 1550 nm plasmonic microcavity photoconductor.** The top electrode consists of a metallic grating of period  $p$ , slit width  $a$  and thickness  $h$ .

The main limitation of existing ultrafast photoconductors is their low level of photoconductance. The low photoconductance is the result of the  $\sim 1\text{-}\mu\text{m}$  absorption length in InGaAs at 1550-nm in combination with the intrinsic electric field inhomogeneity due to the planar geometry of the bias electrodes. (cf. Fig 2a). For an improved electric field distribution both photoconductor thickness ( $t$ ) and electrode spacing ( $L$ ) should be similar and above  $\sim 1\ \mu\text{m}$ . However, for a low-carrier lifetime photoconductor the responsivity is proportional to the photoconductive gain  $\tau/\tau_{tr}$ .<sup>20,22</sup>. Here,  $\tau$  is the carrier lifetime,  $\tau_{tr}$  the transit-time. Thus, a photoconductor with  $\mu\text{m}$ -wide electrode spacing would exhibit a low responsivity and hence low photoconductance, if its carrier lifetime is below 1 ps and its transit time is longer than 10 ps ( $v_{sat} \approx 10^5\text{cm/s}$ ). That is, it can be shown that the photoconductance ( $G_0$ ) of a low-carrier lifetime photoconductor (assuming a 1D geometry) illuminated by an optical beam of power  $P_0$  is equal to<sup>22</sup>:

$$G_0 = A_{InGaAs} \frac{q\mu}{h\nu} \frac{\tau}{L^2} P_0 \quad (2)$$

Eq. (2) shows that a reduction of the electrode spacing increases the photoconductance if the absorption in the InGaAs layer  $A_{InGaAs}$  is kept constant since it increases the carrier density. The capacitance of the photoconductor should also be as low as possible in order to reach THz frequencies. Hence, we define:

$$F = A_{InGaAs} \frac{1}{SL} \frac{q\mu\tau}{\epsilon_r h\nu} \quad (3)$$

as a suitable figure of merit to benchmark the efficiency of photoconductive THz receivers. Here,  $F$  is the ratio of the photoconductance per unit of optical power  $G_0/P_0$  and the electrical capacitance (assuming that  $1/G_0$  remains larger than the load resistance  $R_L \sim 50\ \Omega$ ). For simplicity, the photoconductor is modeled as a parallel plate capacitor with relative dielectric constant  $\epsilon_r$  ( $\epsilon_r = 13.9$  in InGaAs) and area  $S$ . That is, equation (3) shows that reducing the inter-electrode spacing without diminishing the absorption efficiency is a straightforward way to increase  $F$  for a given photoconductive material and active area.

In order to assess the validity of this model, we have investigated photoconductors based on InGaAs:Fe layer embedded in a plasmonic microcavity, as shown schematically in Fig. 2b, with metallic layers acting as bias electrodes and plasmonic waveguide at the same time. The top

electrode is nanostructured to form a grating to achieve efficient coupling of 1550-nm light into the cavity and low parasitic serial resistance<sup>23,24</sup>. The bottom electrode consists of a buried gold layer.

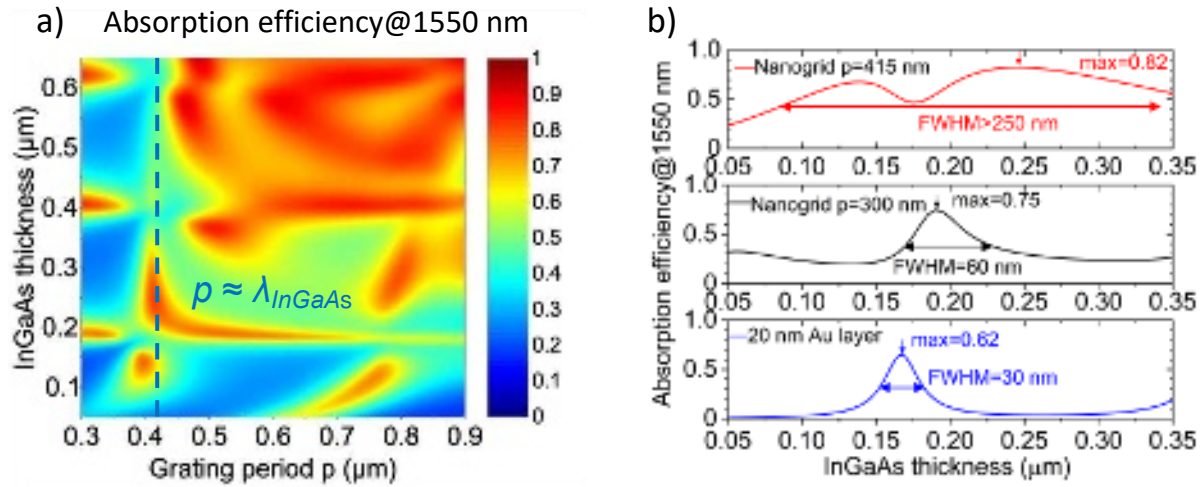


**Fig. 3. (a)** Absorption efficiency map of a plasmonic microcavity photoconductor calculated at 1550 nm by rigorous coupled wave analysis (RCWA) as a function of the grating period  $p$  and InGaAs thickness  $t$  with grating thickness:  $h=300$  nm and slit width  $a=0.3p$ . **(b)** Absorption efficiency vs InGaAs thickness with, from top to bottom panel,  $p=415$  nm,  $p=300$  nm and in the case of a top mirror consisting of 20-nm-thick gold layer cover by a 160-nm-thick Silicon nitride layer. We observe maximum absorption efficiency of 0.82 for  $p=415$  nm (topmost sub-figure) and an InGaAs-thickness of 0.25  $\mu\text{m}$ .

Figure 3a shows a map of the calculated absorption efficiency at 1550-nm-wavelength for a plasmonic microcavity photoconductor (PMP) as a function of the grating period and the InGaAs layer thickness  $t$  (more details can be found in the Methods section). For short grating periods  $p$  below 0.4  $\mu\text{m}$  the absorption efficiency as a function of InGaAs thickness shows narrow absorption peaks related to Fabry-Pérot (FP) resonances. For grating periods longer than the wavelength in InGaAs ( $\lambda_{\text{InGaAs}} \approx 430$  nm), the structure of the absorption efficiency becomes more complex due to diffraction effects. At  $p \approx \lambda_{\text{InGaAs}}$ , the grating can be seen as a coupler of the incident light to the first asymmetric mode of the plasmon slot waveguide<sup>25</sup> leading to a slight dependence on the InGaAs thickness. At  $p \approx 430$  nm and  $t \approx 200$  nm, we can observe an anti-crossing in the absorption map induced by the coupling between these two resonances. Figure 3b depicts the absorption efficiency versus InGaAs thickness at a fixed grating period in the two regimes. Close to the anti-crossing area ( $p = 415$  nm), a very wide absorption peak (FWHM >250 nm) is achieved with a maximum above 80% at 250 nm InGaAs-thickness. For the Fabry-Pérot regime, a narrow peak reaching 75% at  $t \approx 160$  nm with 60-nm-FWHM is predicted. Thus, for microtechnological processing, a very fine control of the InGaAs

layer thickness would be needed – which requires a careful calibration of the growth rates during epitaxy. At the same time, a much narrower spectral absorption bandwidth is calculated for the Fabry-Pérot regime (see figure S2) in comparison to the  $p = 415$  nm case.

As a comparison, we have also calculated the absorption efficiency of a FP cavity with a top mirror consisting of 20-nm of gold covered by a 160-nm-thick silicon nitride (SiN) anti-reflecting (AR) layer, as previously developed for low-temperature-grown GaAs photoconductors operating at 780 nm<sup>26</sup>. In addition to a much larger sheet resistivity, it is shown in Figure 3b (the lowest sub-figure) that the top mirror leads to a lower and narrower absorption efficiency peak. This can be explained by its larger optical losses and its higher reflectance (~60%) despite an optimized SiN AR coating, which prevents achievement of critical coupling condition. Therefore, we decided to disregard this design and move forward with the design of the plasmonic microcavities.

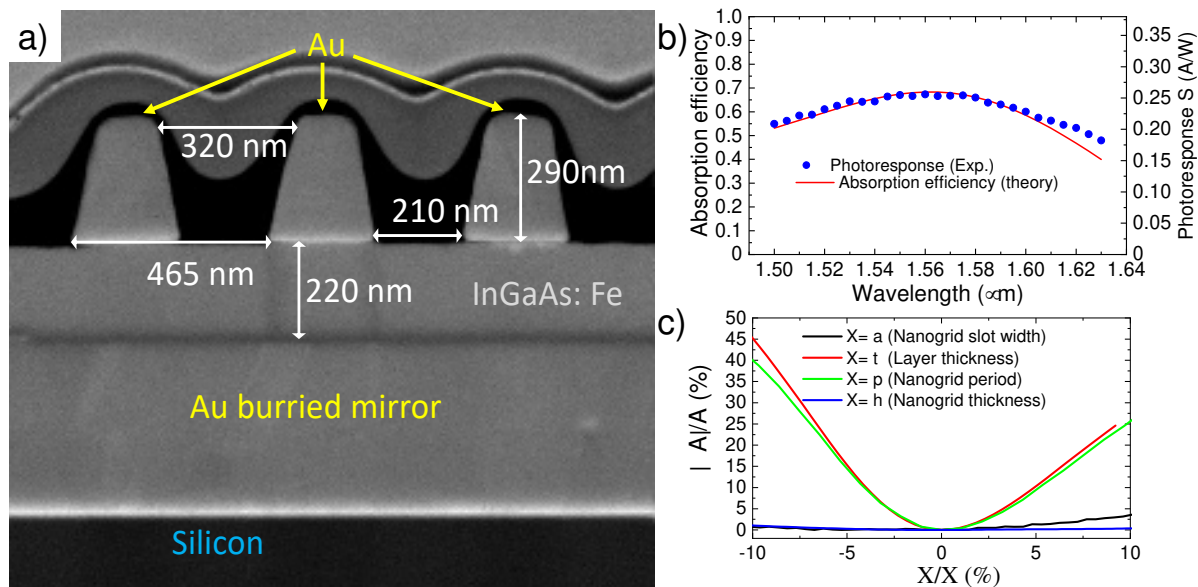


**Fig. 4.** a) SEM view of a FIB-cut cross section of a plasmonic microcavity photoconductor. The measurement uncertainty is around 5 nm. It is worth to notice that the layer above the grating is a Platinum-coating deposited within the FIB chamber and only aimed at protecting the sample from the ion milling. (b) Calculated absorption efficiency using the geometrical parameters measured by SEM and the measured photoresponse obtained from the same device. The scale for the responsivity was chosen to achieve the best visual fit. (c) Relative variation of the absorption efficiency when each parameter is varied around its optimum value, which are  $p = 465$  nm,  $a = 208$  nm;  $t = 217$  nm and  $h = 377$  nm.

Figure 4a shows a scanning electron micrograph of a FIB-cut cross section of a fully processed plasmonic microcavity photoconductor for a set of experimental parameters leading to large absorption around 1550 nm. The buried Au mirror, the InGaAs:Fe absorber and the grating coupler can be clearly seen. The spatial dimensions of the design are indicated in the SEM

image. Figure 4b compares the measured photoresponse as a function of excitation wavelength, which is proportional to the absorption efficiency, (right y-axis) with the calculated absorption efficiency (left y-axis). For the calculation, the parameters as measured by SEM (and shown in Figure 4a) were taken as the input. We observe very good qualitative agreement between measurement and calculation. Figure 4c summarizes the dependencies of the peak absorption efficiency on the geometrical parameters of the plasmonic cavity. In this absorption regime, grating period and layer thickness have a significant and similar impact on the absorption. It would even be possible to counterbalance one with the other during processing.

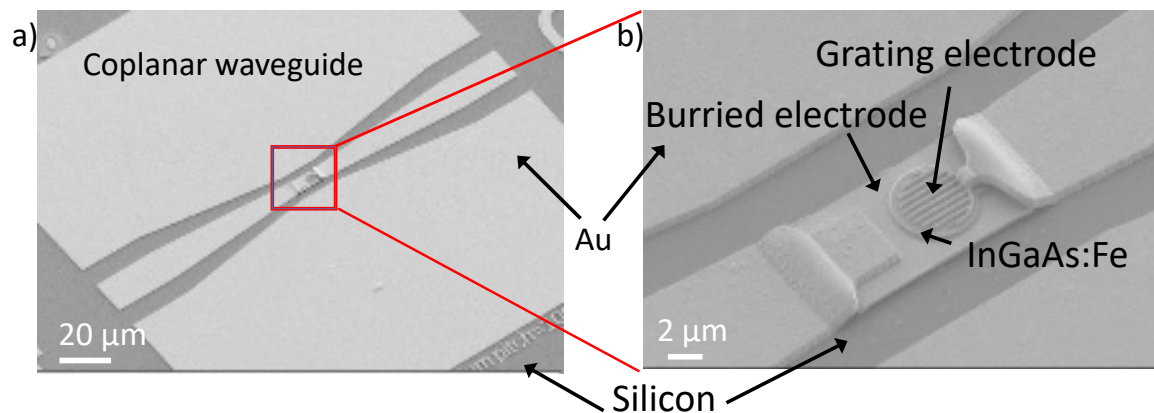


**Fig. 5.** a) SEM view of a plasmonic microcavity photoconductor integrated in series to a coplanar waveguide. b) Close-up of the device showing the top grating electrode, the InGaAs:Fe-layer and the buried back reflector. As can be seen, the absorber is only 5  $\mu\text{m}$  in diameter.

### **Conversion loss measurement up to 320 GHz**

The PMPs are integrated with a coplanar waveguide with contact pads allowing on-wafer characterization. After fabrication, the PMPs were characterized up to 325 GHz. Figure 5 shows SEM views of a typical device integrated in series to a 50-Ohm-coplanar waveguide ended by contact pads with dimensions adapted to the coplanar waveguides used for input and output coupling.

Figure 6a summarizes the I-V characterization of devices with 4- $\mu\text{m}$ -diameter grating-electrodes with and without illumination. It can be noticed that they are not perfectly symmetric with respect to zero bias because of the vertical structure. For optoelectronic mixing applications, this can be easily cancelled by the addition of a small dc bias. When the photoconductor is biased by the THz signal, only the part of the I-V curve around zero is used. In this case the photoconductor can effectively be modeled as a perfect resistor which can be switched from  $R_{off} = 280 \text{ k}\Omega$  to  $R_{on} = 300 \Omega$ , when illuminated by an optical power of 70 mW.

From Eq. 1, a conversion loss of around 20.5 dB is expected if  $R_{on}=300\ \Omega$ . This is in good agreement with the measured conversion loss vs frequency plotted in Figure 6b for devices with top electrode diameter between  $d = 2$  to  $d = 6\ \mu\text{m}$ . The best devices achieve around 22 dB conversion loss at the lower frequencies and around 30 dB at 320 GHz. In comparison, fully packaged state of the art photomixers with integrated antenna show conversion loss of  $\sim 50$  dB at 100 GHz and 60 dB around 300 GHz<sup>17</sup>. It can be seen that the conversion loss is not completely flat even for devices with the smallest diameter devices, whose RC frequency cut-off should be well beyond 300 GHz (1800 GHz for  $d=2$  assuming  $R=50\ \text{Ohm}$ ). However, it is worth noting that the device with  $d=6\ \mu\text{m}$  and  $f_{RC} = 200\ \text{GHz}$  shows, as expected, a larger increase of the conversion losses. We can also see some ripples because of the mismatch between the coplanar probes and the devices. Fig. 6c shows the dynamic range of the detector obtained by sweeping the input power from -60 dBm to 10 dBm. We achieve around 70 dB of dynamic range limited by the experimental set-up. Fig. 6d shows an IF spectrum showing a SNR around 50 dB, despite a very large RBW limited by the laser stability. This shows the superiority of the PMP as a THz mixer in comparison to a photodiode as Ref. <sup>27</sup> reports similar SNR values despite a RBW of 100 Hz, which was possible by using an optical beatnote locked to a RF synthesizer.

### 3. Discussion

The measured conversion loss at frequencies below 70 GHz is in good agreement with the basic model developed in this study. A model allowing the quantitative estimation of the frequency dependent conversion loss would require more extensive work, but it is clear that the cut-off frequency related to the carrier lifetime and the impedance mismatch (due to the electrical capacitance of the device) have the largest impact. In addition, the measured carrier lifetime of the material may not represent the actual carrier lifetime during device operation. This is because the lifetime is deduced from differential transmission measurements, a pump-probe measurement using fs-optical pulses. In contrast, during device operation the photoconductor is illuminated continuously by the optical intensity beating generated by two cw-laser lines. Thus, this carrier lifetime may be quite different due to saturation effects. In our case, the carrier lifetime which should be around 100 fs, resulting in a cut off frequency above 1 THz. However, if the actual lifetime during device operation was around 1 ps instead,

This is the author's peer reviewed, accepted manuscript. However, the online version of record will be different from this version once it has been copyedited and typeset. PLEASE CITE THIS ARTICLE AS DOI: 10.1063/5.0153046

we would obtain a cut-off frequency around 160 GHz, for example. These differences in the measured vs. actual carrier lifetime could explain the increasing conversion loss for higher frequencies for the smallest devices, which exhibit a very low capacitance and high RC cut-off frequency. In addition, developing an accurate electrical model of our conversion loss-measurements is quite difficult, since, as seen before, it will require the perfect knowledge of the source and load impedances on both IF and THz bands. It is not the case, except in the lowest frequency band, since the impedances of the probes and waveguides are known only in their operating frequency band. This could explain the observed ripples and the higher conversion loss for higher frequencies as measured in our experiments.

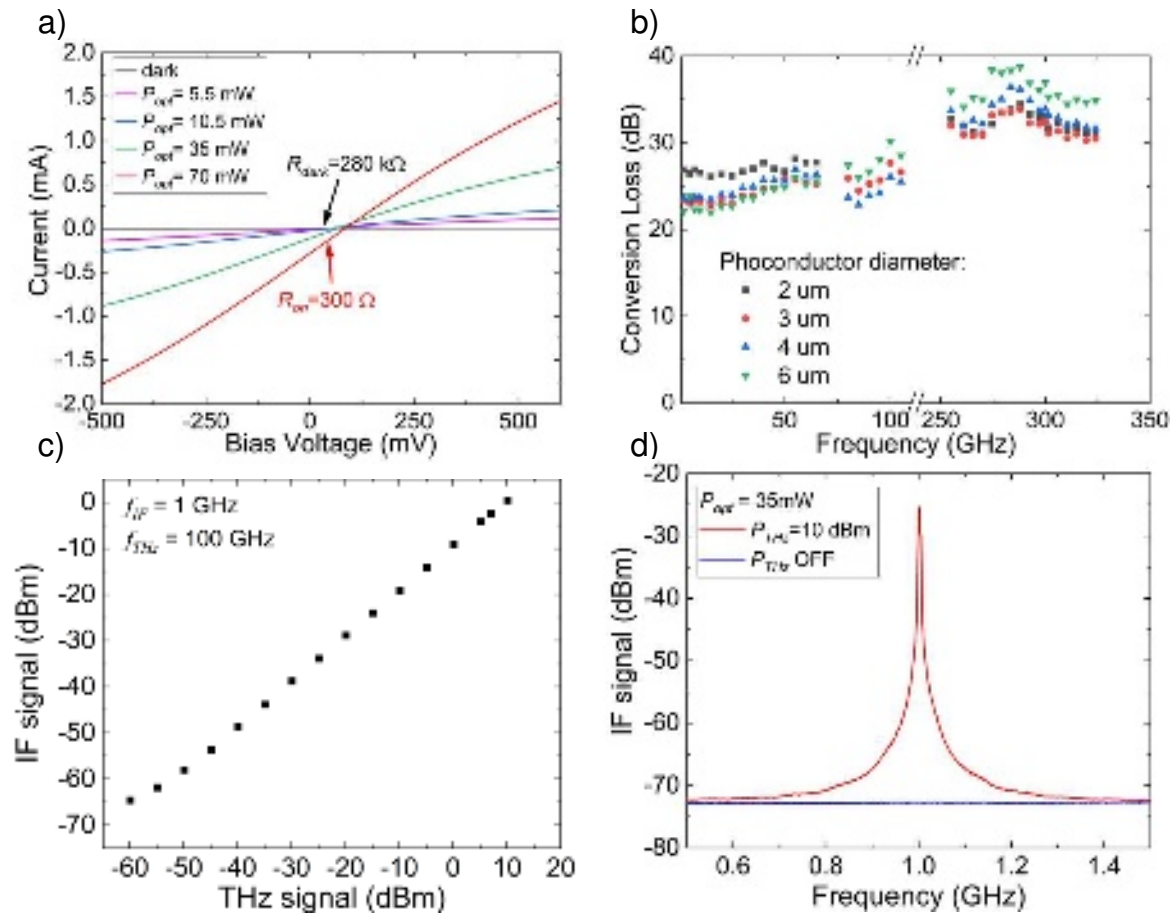


Fig. 6. a) Photocurrent of a 4- $\mu$ m-diameter device vs applied bias voltage for several optical power levels. Around  $V_b=0$  V,  $R_{off}/R_{on} \approx 10^3$  when  $P_{opt}= 70$  mW b) Measured conversion loss vs frequency up to 325 GHz for devices with top electrodes diameters of  $d = 2, 3, 4$  and  $6$   $\mu$ m. The IF frequency was set to  $f_{IF}=1$  GHz and the THz power was  $P_{THz}=-40$  dBm. c) Experimental dynamic range at  $f_{THz}= 100$  GHz ( $P_{opt}= 35$  mW) shown by a 4- $\mu$ m-diameter device. The measurement was limited by the experimental set-up: the resolution bandwidth of the spectrum analyzer was RBW= 3 MHz because of the low spectral stability of the DFB lasers. It results in a noise floor around -70 dBm. On the other side, the maximum THz power was limited to  $P_{THz} \approx 10$  dBm. d) IF spectrum recorded by using a 4- $\mu$ m-diameter device with and without a 100-GHz frequency input signal of 10-dBm-amplitude. Without a THz input signal, the measurement is limited by the noise floor of the spectrum analyzer (RBW=3 MHz).

#### 4. Conclusion

We presented an optoelectronic photomixer based on an ultrafast, MBE-grown InGaAs:Fe layer embedded in a plasmonic microcavity. With this photomixer, we demonstrate a conversion loss as low as  $\sim 30$  dB up to 325 GHz. That is, we expect significantly lower conversion loss than for state-of-the-art photomixers with integrated antenna based on a bulk photoconductive layer, once the PMPs are package. We expect similar improvements beyond 1 THz for the smallest size photomixers (when integrated with a THz antenna), since these devices show RC-related cut-off frequencies reaching 1.8 THz. Further improvements are achievable and will require optimization of the photoconductive material properties as well as better control of the electrical circuit's terminations in both the THz and IF frequency ranges. Overall, the presented plasmonic microcavity photoconductors achieve a very low conversion loss of  $\sim 30$  dB at 320 GHz. This renders these devices extremely promising for application in high-data rate THz communications, in cw-THz spectrometers and in photonics-enabled THz spectrum analyzers.

#### 5. Methods

**Material growth:** For epitaxy, a gas-source molecular beam epitaxy system by Riber was used. The Fe-doped InGaAs layer was grown lattice matched to a semi-insulating, Fe-doped indium phosphide substrate.

**Device Fabrication:** The fabrication of the plasmonic microcavity photodetectors begins with the realization of a buried metal layer acting as the bottom mirror and bottom contact metallization. This is obtained by transferring the epi-layers onto a 2"-diameter high-resistivity ( $>5$  k $\Omega$ .cm) silicon wafer using a Au–Au thermo-compression bonding technique detailed in Ref. <sup>28</sup>, followed by the wet etching of the InP substrate. Next, the Au (300 nm) nanogrid top contact metallization is realized through e-beam lithography, followed by e-beam evaporation and lift-off. The epi-layers are subsequently dry-etched by ICP using the top metal layer as etch-mask. The ground metal layer is finally dry-etched by an Ar<sup>+</sup> ion-beam around the PMP's down to the silicon substrate (Fig. 5). To electrically connect the nanogrid to the 50  $\Omega$  coplanar line, suspended Ti/Au (20 nm/600 nm) wire-bridges are finally fabricated by a two-step e-beam lithography process. To this end, a first resist layer is used as support after deposition, e-beam lithography and reflow, followed by a second one to define the wires by

standard lift-off process. The same process is used to realize the air-bridge connecting the 2D array to the  $50 \Omega$  coplanar line.

### **Optical simulation of the plasmonic microcavity photoconductor**

The numerical simulations are carried out to calculate the absorption efficiency of the PMPs. We define the absorption efficiency as the ratio of the absorbed power in the InGaAs-layer to the incident optical power, as a function of the nanogrid period  $p$ , aperture width  $a$ , and cavity thickness  $t$ . The cavity is considered as a 2D structure infinitely periodic along one dimension and infinitely long on the other one (see Fig. 2(b)). The system is illuminated under normal incidence with a plane wave polarized orthogonally to the nanogrid electrodes (shown in Fig. 2b.). Frequency-dependent dielectric functions have been taken from Ref. <sup>29</sup> (In<sub>53</sub>Ga<sub>47</sub>As) and Ref. <sup>30</sup> (Au).

### **Photoresponse spectrum measurement.**

Photoresponse spectrum of the PMP's was conducted by illuminating a test structure of  $20 \times 20 \mu\text{m}^2$  area by an external-cavity laser (Yenista Tunics) by using a lensed optical fiber of mode field diameter (MFD) equal to  $3 \mu\text{m}$ . Photoresponse data are directly extracted from the photocurrent measured by a sourcemeter (Keithley 2612A) at a bias voltage of 4 V and 4.2 mW of incident power under TM polarization.

### **Conversion Loss measurement:**

A schematic of the photomixing measurement set-up is shown in Fig. S3 ([Supplementary Material](#)). The optical beatnote is generated by spatially overlapping the emission of two fiber-coupled DFB laser diodes (TOPTICA) by means of a 50:50 polarization maintaining fiber coupler. This beatnote is then amplified by an Erbium-doped fiber amplifier (Lumibird). The wavelengths of the DFBs are close to 1550 nm and are measured by an OSA with a 1-GHz-accuracy. The optical beatnote is then focused on the device by a lensed fiber providing a Gaussian beam spot with a minimum width of around  $3 \mu\text{m}$ . Below 67 GHz, the signal is provided by a microwave synthesizer (Agilent E8257D). In the 75 - 110 GHz and 220 - 325 GHz frequency bands the signal is provided by a X3 and X9 multiplier chain (VDI SGX) driven by the same microwave synthesizer. In each frequency band coplanar probes are used to transmit the signal to the device through the  $50\text{-}\Omega$  coplanar line. The dynamic range at 100 GHz was measured by means of a calibrated attenuator enabling to tune the incoming power from -50 dBm to 10 dBm.

In all cases, the mixing signal generated at the intermediate frequency  $f_{IF}$  is outcoupled by a 0 – 67 GHz coplanar probe and sent after amplification through a bias-T to a spectrum analyzer (SA). The measured power levels,  $P_{IF}$  and  $P_{THz}$ , are corrected for losses induced by the coplanar probes and by the waveguides and coaxial cables. They reach 1.5 dB for the IF power, 1.4 dB around 100 GHz and  $\sim 4$  dB at 300 GHz for the THz power. At each THz frequency, the beating frequency is adjusted to ensure  $f_{IF} = 1$  GHz.

### SUPPLEMENTARY MATERIALS

The supporting information includes a circuit model of the optoelectronic mixing in a photoconductor, additional simulation data of the absorption efficiency of the plasmonic microcavity photoconductors and a schematic of the experimental set-up.

### ACKNOWLEDGEMENTS

This work was supported by Hauts de France Regional Council (CPER “Wavetech”, Start-AIRR ASPIR), RENATECH (French Network of Major Technology Centres), and French National Research Agency (Project BIRD, TIGER, PEPR Electronics)

### AUTHOR DECLARATIONS

#### Conflict of Interest

The authors have no conflicts to disclose.

**Author Contributions.** C.T. and V.M. contributed equally to the work. E.P. made the design of optical cavities. S.B. performed the Fe:InGaAs layer growth. V.M. and C.T. fabricated the samples under the supervision of E.P. and G. Di. C.T. and V.M. measured the dc photoresponse vs wave-length. S.B. G.D. and V.A. built the experimental set-up for the ac optoelectronic measurements. E.P. C.T. and V.M. performed the heterodyne detection measurement. E.P. and J-F.L. derived the equivalent circuit model. C.T, V.M., R.K, B.G and E.P. discussed and analyzed the results. E.P. and R.K. wrote the manuscript with contributions from C.T, V.M, G.D., V.A., S.B. and G.Di.. R.K. and E.P. supervised the project.

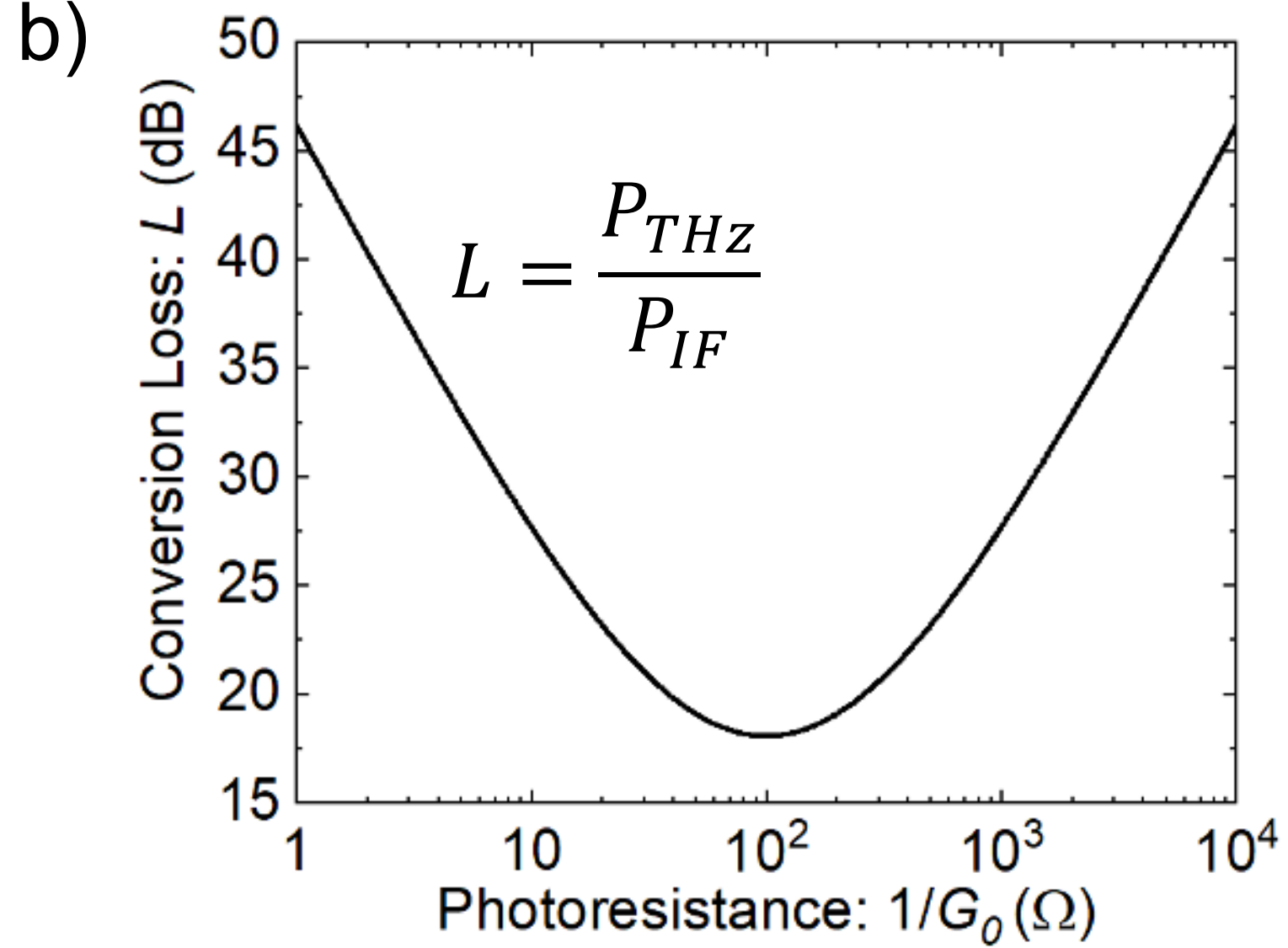
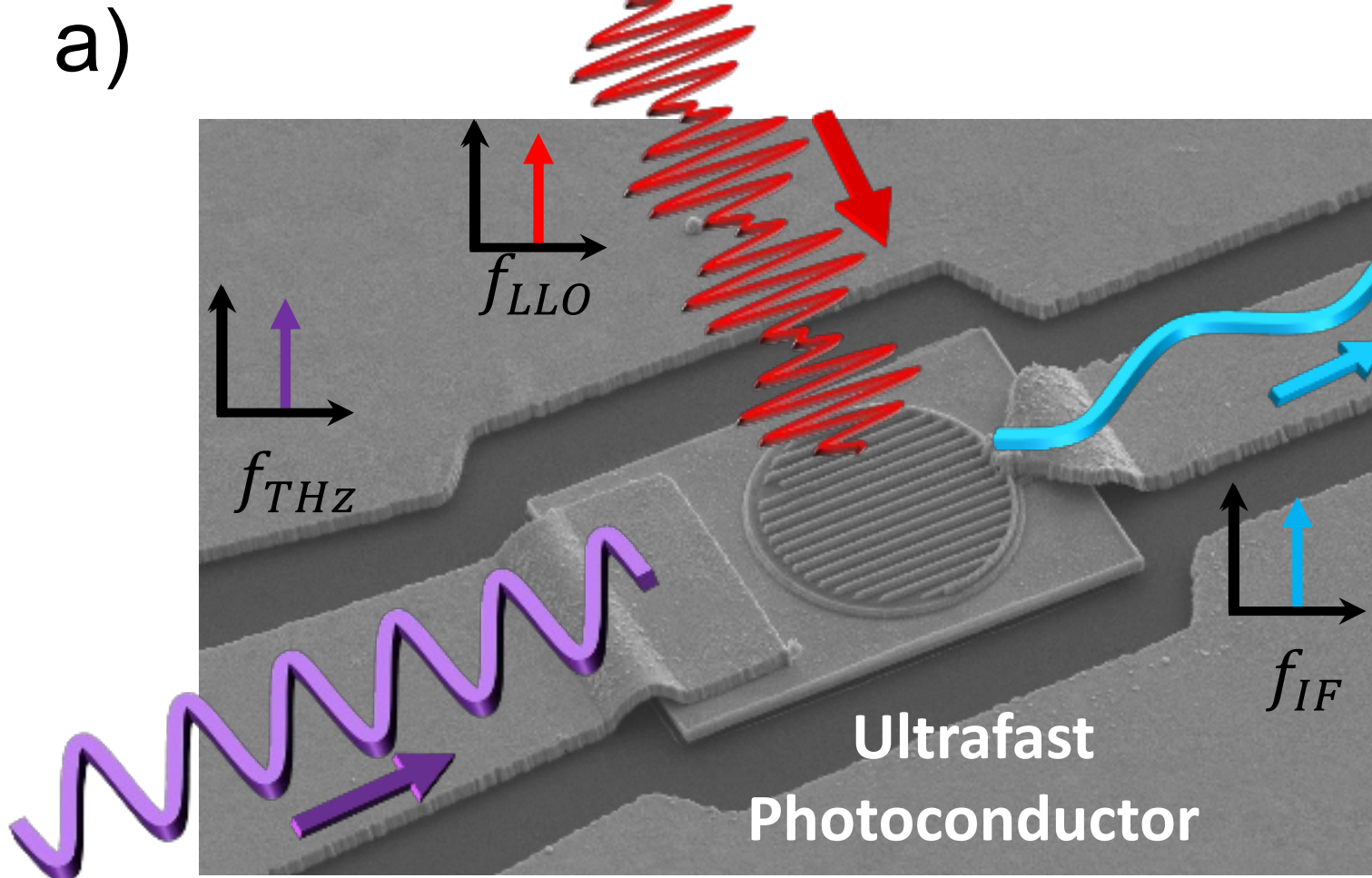
### References

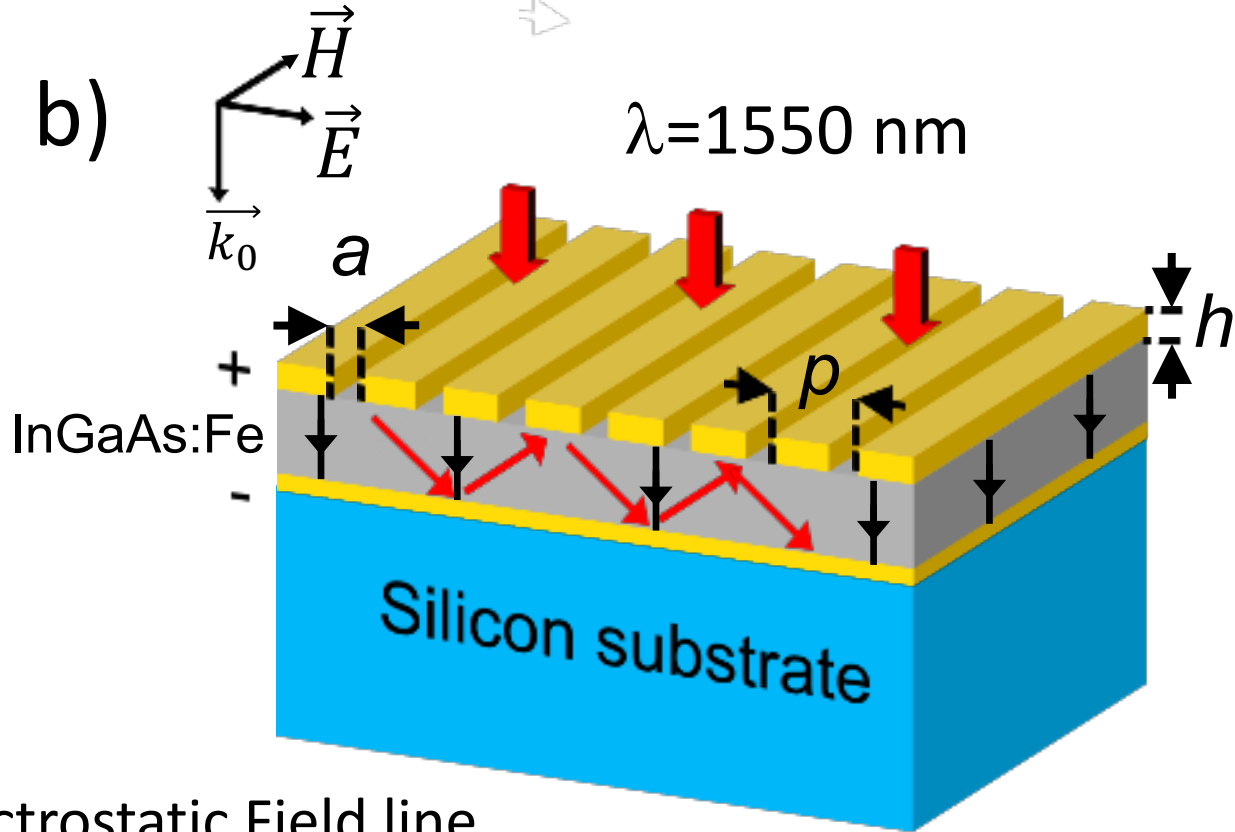
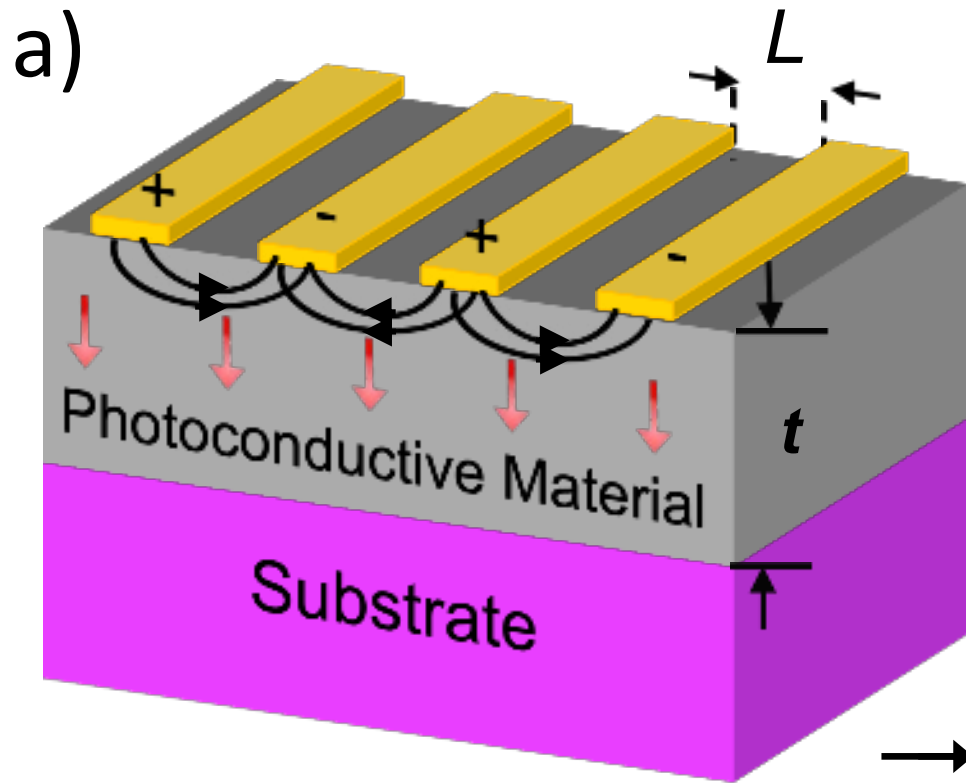
- [1] Schlecht, E.; Siles, J. V.; Lee, C.; Lin, R.; Thomas, B.; Chattopadhyay, G.; Mehdi, I. Schottky Diode Based 1.2 THz Receivers Operating at Room-Temperature and below for Planetary Atmospheric Sounding. *IEEE Trans. Terahertz Sci. Technol.* **2014**, *4* (6), 661–669. <https://doi.org/10.1109/TTHZ.2014.2361621>.
- [2] Siegel, P. H. Terahertz Technology. *IEEE Trans. Microw. Theory Tech.* **2002**, *50* (3), 910–928.

- <https://doi.org/10.1109/22.989974>.
- (3) Siegel, P. H. THz Instruments for Space. *IEEE Trans. Antennas Propag.* **2007**, *55* (11 1), 2957–2965. <https://doi.org/10.1109/TAP.2007.908557>.
  - (4) Liebermeister, L.; Nellen, S.; Kohlhaas, R.; Breuer, S.; Schell, M.; Globisch, B. Ultra-Fast, High-Bandwidth Coherent Cw THz Spectrometer for Non-Destructive Testing. *J. Infrared, Millimeter, Terahertz Waves* **2019**, 1–9. <https://doi.org/10.1007/s10762-018-0563-6>.
  - (5) Roggenbuck, A.; Schmitz, H.; Deninger, A.; Mayorga, I. C.; Hemberger, J.; Güsten, R.; Grüniger, M. Coherent Broadband Continuous-Wave Terahertz Spectroscopy on Solid-State Samples. *New J. Phys.* **2010**, *12* (4), 043017. <https://doi.org/10.1088/1367-2630/12/4/043017>.
  - (6) Nagatsuma, T.; Ducournau, G.; Renaud, C. C. Advances in Terahertz Communications Accelerated by Photonics. *Nat. Photonics* **2016**, *10* (6), 371–379. <https://doi.org/10.1038/nphoton.2016.65>.
  - (7) Verghese, S.; McIntosh, K. A.; Calawa, S.; Dinatale, W. F.; Duerr, E. K.; Molvar, K. A. Generation and Detection of Coherent Terahertz Waves Using Two Photomixers. *Appl. Phys. Lett.* **1998**, *73* (26), 3824. <https://doi.org/10.1063/1.122906>.
  - (8) Loas, G.; Romanelli, M.; Alouini, M. Dual-Frequency 780-Nm Ti:Sa Laser for High Spectral Purity Tunable CW THz Generation. *IEEE Photonics Technol. Lett.* **2014**, *26* (15), 1518–1521. <https://doi.org/10.1109/LPT.2014.2327656>.
  - (9) Rolland, A.; Ducournau, G.; Loas, G.; Peytavit, E.; Beck, A.; Akalin, T.; Zaknounge, M.; Lampin, J.-F.; Brunei, M.; Bondu, F.; Vallet, M.; Alouini, M. Narrow Linewidth Tunable THz Signal Radiated by Photomixing: Coupling a Unitravelling Carrier Photodiode and a Two-Axis Dual-Frequency Laser. In *2012 Conference on Lasers and Electro-Optics, CLEO 2012*; 2012.
  - (10) Latkowski, S.; Parra-Cetina, J.; Maldonado-Basilio, R.; Landais, P.; Ducournau, G.; Beck, A.; Peytavit, E.; Akalin, T.; Lampin, J.-F. Analysis of a Narrowband Terahertz Signal Generated by a Unitravelling Carrier Photodiode Coupled with a Dual-Mode Semiconductor Fabry-Pérot Laser. *Appl. Phys. Lett.* **2010**, *96* (24). <https://doi.org/10.1063/1.3447931>.
  - (11) Hallal, A.; Bouhier, S.; Bondu, F. Frequency Stabilization of a Laser Tunable over 1 THz in an All Fibered System. *IEEE Photonics Technol. Lett.* **2016**, *28* (11), 1249–1252. <https://doi.org/10.1109/LPT.2016.2532119>.
  - (12) Ito, H.; Song, H.-J.; Suizu, K.; Shimizu, N.; Nagatsuma, T.; Furuta, T. Broadband-Frequency-Tunable Sub-Terahertz Wave Generation Using an Optical Comb, AWGs, Optical Switches, and

- This is the author's pre-reviewed accepted manuscript. However, the online version of the record will be different from this version once it has been copyedited and typeset.  
PLEASE CITE THIS ARTICLE AS DOI: 10.1063/5.0153046
- a Uni-Traveling Carrier Photodiode for Spectroscopic Applications. *J. Light. Technol.* Vol. 26, Issue 15, pp. 2521-2530 **2008**, 26 (15), 2521–2530.
- (13) Tetsumoto, T.; Ayano, F.; Yeo, M.; Webber, J.; Nagatsuma, T.; Rolland, A. 300 GHz Wave Generation Based on a Kerr Microresonator Frequency Comb Stabilized to a Low Noise Microwave Reference. *Opt. Lett.* **2020**, 45 (16), 4377. <https://doi.org/10.1364/ol.398345>.
- (14) Göbel, T.; Stanze, D.; Globisch, B.; Dietz, R. J. B.; Roehle, H.; Schell, M. Telecom Technology Based Continuous Wave Terahertz Photomixing System with 105 Decibel Signal-to-Noise Ratio and 35 Terahertz Bandwidth. *Opt. Lett.* **2013**, 38 (20), 4197. <https://doi.org/10.1364/OL.38.004197>.
- (15) Mohandas, R. A.; Freeman, J. R.; Rosamond, M. C.; Hatem, O.; Chowdhury, S.; Ponnampalam, L.; Fice, M.; Seeds, A. J.; Cannard, P. J.; Robertson, M. J.; Moodie, D. G.; Cunningham, J. E.; Davies, A. G.; Linfield, E. H.; Dean, P. Generation of Continuous Wave Terahertz Frequency Radiation from Metal-Organic Chemical Vapour Deposition Grown Fe-Doped InGaAs and InGaAsP. *J. Appl. Phys.* **2016**, 119 (15), 153103. <https://doi.org/10.1063/1.4946845>.
- (16) Deumer, M.; Breuer, S.; Kohlhaas, R.; Nellen, S.; Liebermeister, L.; Lauck, S.; Schell, M.; Schell, M.; Globisch, B.; Globisch, B. Continuous Wave Terahertz Receivers with 4.5 THz Bandwidth and 112dB Dynamic Range. *Opt. Express, Vol. 29, Issue 25, pp. 41819-41826* **2021**, 29 (25), 41819–41826. <https://doi.org/10.1364/OE.443098>.
- (17) Harter, T.; Ummethala, S.; Blaicher, M.; Muehlbrandt, S.; Wolf, S.; Weber, M.; Adib, M. M. H.; Kemal, J. N.; Merboldt, M.; Boes, F.; Nellen, S.; Tessmann, A.; Walther, M.; Globisch, B.; Zwick, T.; Freude, W.; Randel, S.; Koos, C. Wireless THz Link with Optoelectronic Transmitter and Receiver. *Optica* **2019**, 6 (8), 1063. <https://doi.org/10.1364/optica.6.001063>.
- (18) Nellen, S.; Globisch, B.; O’Gorman, J.; Anthur, A. P.; Vujicic, V.; Barry, L.; Schell, M. Fiber-Coupled, Photoconductive Receiver for Heterodyne Detection up to 1 THz Stabilized by an Optical Frequency Comb. In *International Conference on Infrared, Millimeter, and Terahertz Waves, IRMMW-THz*; IEEE Computer Society, 2017. <https://doi.org/10.1109/IRMMW-THz.2017.8067019>.
- (19) Coleman, P. D.; Eden, R. C.; Weaver, J. N. Mixing and Detection of Coherent Light. *IEEE Trans. Electron Devices* **1964**, ED-11 (11), 488–497. <https://doi.org/10.1109/T-ED.1964.15371>.
- (20) Peytavit, E.; Ducournau, G.; Lampin, J.-F. THz Photomixers. In *Fundamentals of Terahertz Devices and Applications*; John Wiley & Sons, Ltd, 2021; pp 137–186. <https://doi.org/10.1002/9781119460749.CH4>.

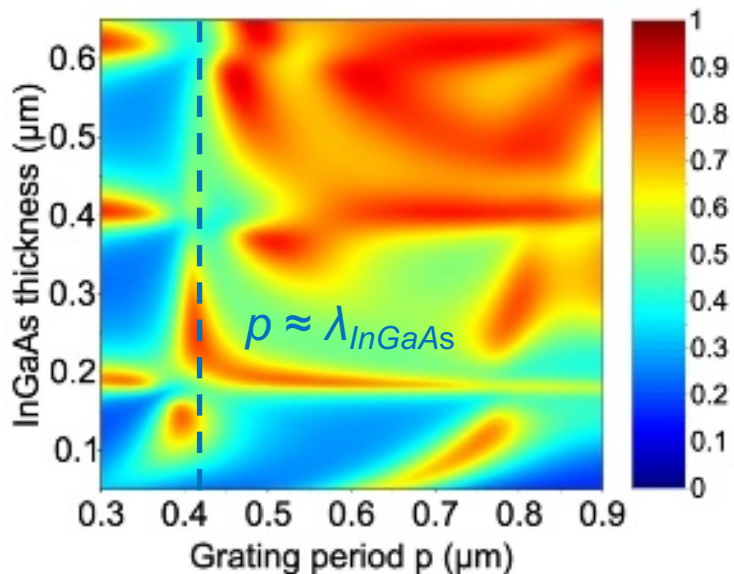
- This is the author's peer reviewed, accepted manuscript. However, the online version of record will be different from this version once it has been copy edited and typeset. PLEASE CITE THIS ARTICLE AS DOI: 10.1063/1.53046
- [21] Kelly, A. J. Fundamental Limits on Conversion Loss of Double Sideband Resistive Mixers. *IEEE Trans. Microw. Theory Tech.* **1977**, 25 (11), 867–869. <https://doi.org/10.1109/TMTT.1977.1129233>.
- [22] Rosencher, E.; Vinter, B. *Optoelectronics*; Cambridge University Press, 2002.
- [23] Billet, M.; Desmet, Y.; Coinon, C.; Ducoumau, G.; Wallart, X.; Lampin, J. F.; Peytavit, E. Ultra-Thin InGaAs-MSM Photodetectors for THz Optoelectronics Applications. In *International Conference on Infrared, Millimeter, and Terahertz Waves, IRMMW-THz*; 2017. <https://doi.org/10.1109/IRMMW-THz.2017.8067020>.
- [24] Billet, M.; Desmet, Y.; Bavedila, F.; Barbieri, S.; Hänsel, W.; Holzwarth, R.; Ducournau, G.; Lampin, J.-F.; Peytavit, E. Sub-Sampling of RF and THz Waves Using LT-GaAs Photoconductors under 1550 Nm Light Excitation. *Electron. Lett.* **2017**, 53 (24), 1596–1598. <https://doi.org/10.1049/el.2017.2769>.
- [25] Dionne, J. A.; Sweatlock, L. A.; Atwater, H. A.; Polman, A. Plasmon Slot Waveguides: Towards Chip-Scale Propagation with Subwavelength-Scale Localization. *Phys. Rev. B - Condens. Matter Mater. Phys.* **2006**, 73 (3), 1–9. <https://doi.org/10.1103/PhysRevB.73.035407>.
- [26] Peytavit, E.; Lepilliet, S.; Hindle, F.; Coinon, C.; Akalin, T.; Ducournau, G.; Mouret, G.; Lampin, J.-F. Milliwatt-Level Output Power in the Sub-Terahertz Range Generated by Photomixing in a GaAs Photoconductor. *Appl. Phys. Lett.* **2011**, 99 (22), 223508. <https://doi.org/10.1063/1.3664635>.
- [27] Rouvalis, E.; Fice, M.; Renaud, C.; Seeds, A. Millimeter-Wave Optoelectronic Mixers Based on Uni-Travelling Carrier Photodiodes. *IEEE Trans. Microw. Theory Tech.* **2012**, 60 (3), 686–691.
- [28] Peytavit, E.; Lampin, J.-F.; Hindle, F.; Yang, C.; Mouret, G. Wide-Band Continuous-Wave Terahertz Source with a Vertically Integrated Photomixer. *Appl. Phys. Lett.* **2009**, 95 (16), 161102. <https://doi.org/10.1063/1.3251071>.
- [29] Seifert, S.; Runge, P. Revised Refractive Index and Absorption of In<sub>1-x</sub>Ga<sub>x</sub>As<sub>y</sub>P<sub>1-y</sub> Lattice-Matched to InP in Transparent and Absorption IR-Region. *Opt. Mater. Express* **2016**, 6 (2), 629. <https://doi.org/10.1364/ome.6.000629>.
- [30] Arsenin, A. V.; Yakubovsky, D. I.; Fedyanin, D. Y.; Volkov, V. S.; Stebunov, Y. V. Optical Constants and Structural Properties of Thin Gold Films. *Opt. Express, Vol. 25, Issue 21, pp. 25574-25587* **2017**, 25 (21), 25574–25587. <https://doi.org/10.1364/OE.25.025574>.





- Electrostatic Field line
- Light rays

a) Absorption efficiency@1550 nm



b)

